Experimental Validation of a CFD-Based Blade Element Theory Disk Model for a Small Quadrotor UAV

Junzhe Liu*
Vanderbilt University / Summer Intern, Flexcompute Inc.

Qiqi Wang†
Associate Professor, MIT / Co-Founder, Flexcompute Inc.

This paper presents an experimental validation of a computational fluid dynamics (CFD) workflow incorporating a blade element theory (BET) disk model for predicting the aerodynamic performance of a small quadrotor unmanned aerial vehicle (UAV). A Parrot Anafi 4K drone was used as the test platform. A simplified geometric model was constructed based on manufacturer-provided CAD data, and rotor blade aerodynamics were characterized using two-dimensional airfoil analysis. Physical flight experiments were conducted in a controlled indoor environment, and onboard telemetry data were used to extract velocity and acceleration histories under prescribed forward pitch angles. Numerical simulations were performed using a steady-state CFD solver with BET disk representations of the rotors. Simulated results were compared against both experimental flight data and a physics-based simulation environment. The BET disk model was found to accurately capture overall acceleration–velocity trends across multiple flight conditions, while underpredicting acceleration magnitude due to modeling assumptions and steady-state limitations.

I. Introduction

Small quadrotor unmanned aerial vehicles (UAVs) operate in low-Reynolds-number flow regimes where aerodynamic performance is strongly influenced by rotor–airframe interaction and transient propulsion effects. While blade-resolved computational fluid dynamics (CFD) simulations can capture detailed flow physics, their computational cost limits their use in iterative design workflows. Reduced-order rotor models, such as blade element theory (BET) disk approaches, are therefore widely employed for engineering analysis.

Despite their popularity, BET disk models rely on simplifying assumptions that neglect blade-scale unsteadiness and detailed wake dynamics. Experimental validation is essential to assess the accuracy and applicability of such models for small UAV configurations. This study aims to validate a BET disk CFD workflow by comparing numerical predictions with controlled flight measurements from a commercial quadrotor platform.

II. Materials and Methods

A. UAV Geometry and Simplified Modeling

The Parrot Anafi 4K quadrotor was selected as the test platform. Manufacturer-provided CAD geometry was used as a reference to construct a simplified model suitable for CFD analysis. Overall dimensions and geometric angles were preserved, while small features such as holes, internal structures, and the onboard camera were removed. Certain components, including the landing supports, were replaced with simplified geometric primitives. This approach preserved the external aerodynamic shape while enabling robust meshing.

B. Rotor Blade Geometry and Airfoil Analysis

Each rotor blade has a length of approximately 60 mm. A physical blade was three-dimensionally scanned, and cross sections were extracted at multiple radial locations along the blade span. Cross-sectional profiles were generated at selected radii and exported as DXF files. A custom Python script was developed to convert the profiles into airfoil data files, normalize orientation, and extract local twist and chord distributions.

*Undergraduate Student, Vanderbilt University, AIAA University Student Member 1924096
†Associate Professor, MIT, AIAA Associate Fellow.

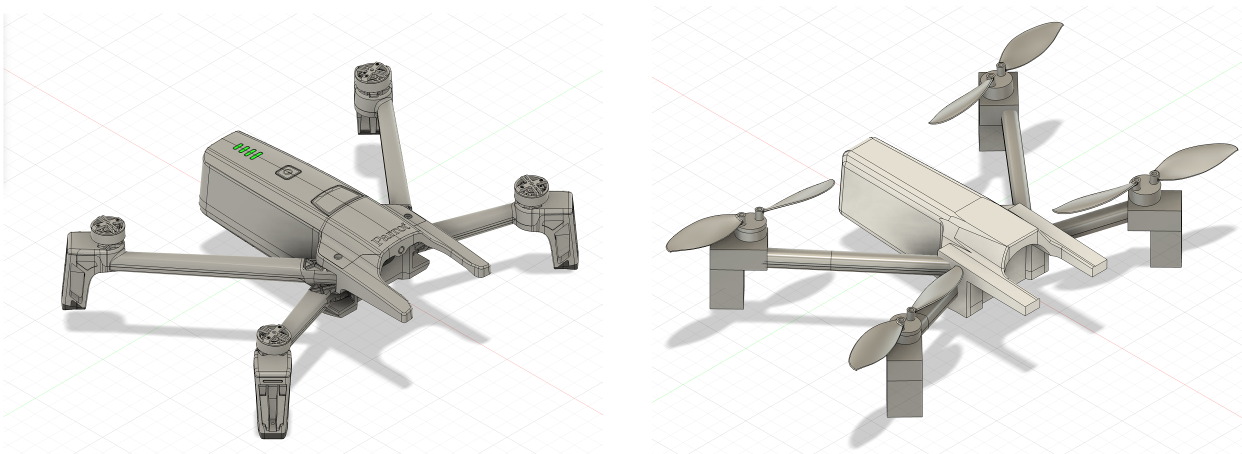

(a) Manufacturer-provided CAD geometry **(b) Simplified CFD geometry used in simulations**

Fig. 1 Comparison between the manufacturer-provided CAD model and the simplified geometry used for CFD simulations. The propellers are assembled from 3D scan.

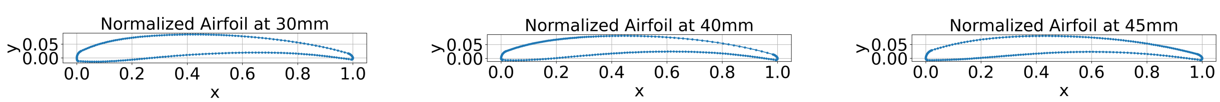

(a) $r = 30\,\text{mm}$ **(b)** $r = 40\,\text{mm}$ **(c)** $r = 45\,\text{mm}$

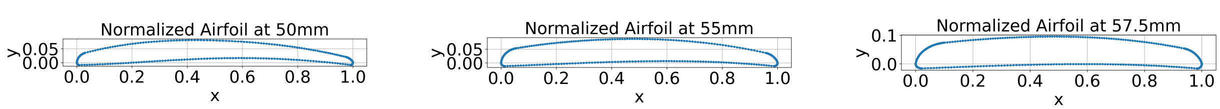

(d) $r = 50\,\text{mm}$ **(e)** $r = 55\,\text{mm}$ **(f)** $r = 57.5\,\text{mm}$

Fig. 2 Normalized airfoil cross sections extracted from the scanned rotor blade at selected radial locations. Profiles were aligned and normalized prior to aerodynamic analysis using XFOIL.

Linear and quadratic fits were applied to the twist and chord distributions, respectively. Based on aerodynamic relevance, only the airfoil sections at $r = 30$ mm, 45 mm, and 55 mm were retained for aerodynamic analysis.

Two-dimensional airfoil polars were generated using XFOIL over an angle-of-attack range of $-15°$ to $15°$. Reynolds numbers were selected based on local blade radius and operating conditions, with representative values of $Re \approx 4.5\times10^4$, 4.0×10^4, and 6.0×10^3. Transition thresholds of $N_{\text{crit}} = 0.02$ were applied on both suction and pressure sides to improve convergence.

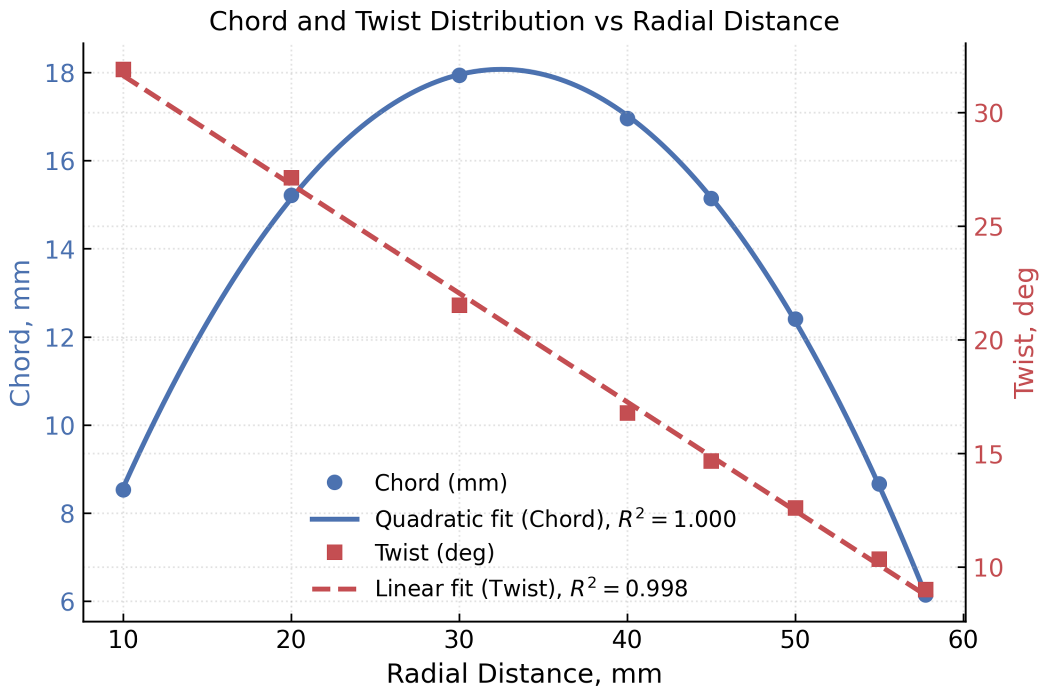

Fig. 3 Chord and twist distributions extracted from the scanned rotor blade and fitted using $c(r) = a_c r^2 + b_c r + c_c$ (quadratic chord fit) and $\theta(r) = a_\theta r + b_\theta$ (linear twist fit), where r is the radial distance from the blade root.

C. Extraction of XROTOR Aerodynamic Parameters

Lift and drag coefficient outputs from XFOIL were post-processed to obtain a reduced set of aerodynamic parameters suitable for blade-element momentum analysis. In the linear lift regime, the lift coefficient was approximated as

$$C_L(\alpha) = \frac{dC_L}{d\alpha}(\alpha - \alpha_0), \tag{1}$$

where α_0 is the zero-lift angle of attack and $dC_L/d\alpha$ is the lift slope.

Positive and negative stall limits, $C_{L,\max}$ and $C_{L,\min}$, were extracted directly from the extrema of the XFOIL polars. The drag polar was approximated using a quadratic form,

$$C_D = C_{D,\min} + k\left(C_L - C_{L,\min D}\right)^2, \tag{2}$$

where $C_{D,\min}$ is the minimum drag coefficient, $C_{L,\min D}$ is the lift coefficient at minimum drag, and k is the quadratic drag coefficient. All aerodynamic parameters derived from the XFOIL polars, including the zero-lift angle α_0, lift slope $\mathrm{d}C_L/\mathrm{d}\alpha$, stall limits $C_{L,\max}$ and $C_{L,\min}$, minimum drag coefficient $C_{D,\min}$, lift coefficient at minimum drag $C_{L,\min D}$, and quadratic drag coefficient k were directly written into the XROTOR input file and used without further tuning in the subsequent blade-element and CFD simulations.

This parameterization provides a compact representation of the airfoil aerodynamic behavior suitable for use in XROTOR and BET disk simulations.

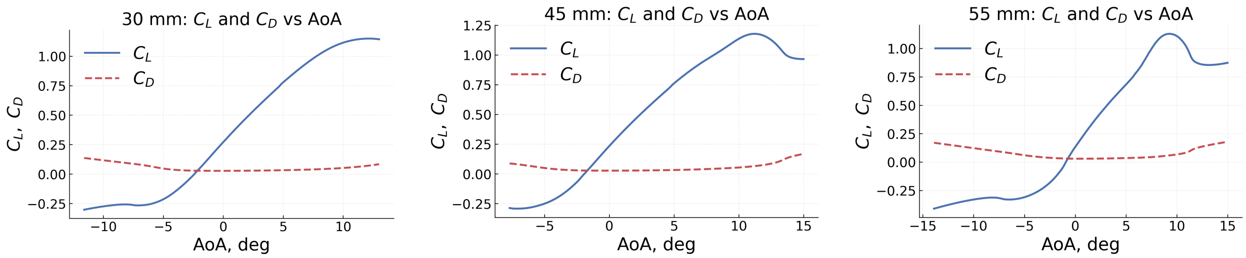

(a) $r = 30\,\text{mm}$ **(b)** $r = 45\,\text{mm}$ **(c)** $r = 55\,\text{mm}$

Fig. 4 Lift and drag coefficient polars obtained from XFOIL for the three blade sections used in the blade-element analysis. Each panel shows C_L and C_D as functions of angle of attack.

D. Flight Experiments

Flight experiments were conducted in a large indoor hall to minimize environmental disturbances. The drone was controlled using the Parrot API to maintain fixed forward pitch angles of 2°, 5°, and 10°, after which it was allowed to accelerate freely. Onboard telemetry data were recorded, including velocity, acceleration, and motor rotational speed. For each pitch angle, three independent flight runs were conducted, and the resulting measurements were averaged to obtain the reported data.

The same control logic was also executed in the Parrot Sphinx simulation environment, where a manufacturer-provided drone model generates simulated telemetry outputs comparable to those obtained from physical flight, providing a closely matched reference for comparison.

The drone mass was assumed constant and obtained from manufacturer specifications. Motor speed data were extracted directly from flight telemetry and processed by averaging three consecutive data points within quasi-steady acceleration intervals for each operating condition. The corresponding freestream velocity was obtained from the same flight segments. Front and rear propulsion units were treated separately, with independent time-averaged rotational speeds assigned to each motor set to reflect asymmetric operating conditions observed in flight. As a result, each simulated case was defined by a unique combination of flight-measured airspeed and independently averaged front and rear motor rotational speeds for a given pitch condition. The resulting motor speeds spanned a range of approximately 8,000–10,000 RPM and were applied directly as inputs to the CFD simulations, rather than assuming a single nominal rotational speed.

E. CFD Simulation Setup

Numerical simulations were performed with a steady-state formulation using Flow360, a commercial CFD solver developed by Flexcompute Inc. Each rotor was modeled using a BET disk representation, with four counter-rotating disks corresponding to the physical quadrotor configuration. Thrust generated by each disk was computed directly by the solver.

The net streamwise force acting on the vehicle was computed as

$$F_x = \sum_{i=1}^{4} T_i - D_{\text{body}}, \tag{3}$$

where T_i is the thrust generated by the i-th rotor disk and D_{body} is the integrated aerodynamic drag on the airframe. For each pitch angle, six forward velocity conditions were simulated. The simulation for each operating condition converged in less than five minutes.

III. Results and Discussion

Acceleration–velocity comparisons for pitch angles of 2°, 5°, and 10° show consistent trends across experimental flight data, Sphinx simulation results, and CFD predictions. In all cases, acceleration decreases monotonically with increasing velocity due to the balance between thrust and aerodynamic drag.

The BET disk CFD simulations capture the overall slope and qualitative shape of the measured acceleration–velocity relationship but systematically underpredict the acceleration magnitude across the operating envelope. Agreement

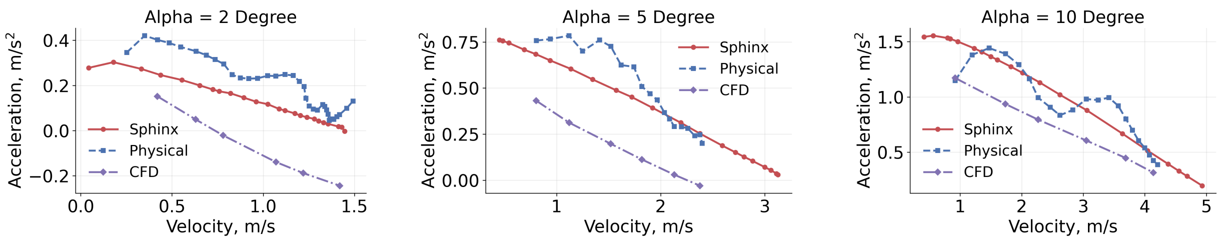

(a) $\alpha = 2°$ **(b)** $\alpha = 5°$ **(c)** $\alpha = 10°$

Fig. 5 Comparison of acceleration as a function of forward velocity for experimental flight data, Parrot Sphinx simulation, and BET disk CFD predictions at three commanded pitch angles.

improves at higher pitch angles, where thrust dominates drag and relative modeling error is reduced. Despite quantitative offsets, the CFD results successfully reproduce the correct aerodynamic trends across all test conditions.

One contributing source of error is uncertainty in the motor rotational speed inputs derived from flight telemetry. Although RPM values were time-averaged over short quasi-steady intervals, residual unsteadiness remains due to rapidly evolving flight conditions, motor control transients, and sensor noise, all of which can introduce discrepancies between the effective in-flight rotor state and the steady RPM prescribed in the CFD model. Additional sources of underprediction stem from the steady-state nature of the BET formulation and the omission of transient motor and controller dynamics that can temporarily enhance thrust during acceleration. In contrast, the Sphinx flight simulator is calibrated using post-build experimental data and vehicle-specific system identification, allowing it to implicitly capture propulsion, control, and aerodynamic coupling effects that are difficult to model a priori. While this calibration yields higher predictive accuracy for the as-built vehicle, CFD retains the distinct advantage of enabling performance estimation prior to hardware fabrication, making it a complementary tool rather than a replacement for flight-calibrated simulation.

A. Flow-field visualization and interpretation

In addition to the kinematic validation, representative flow-field outputs were examined to provide qualitative insight into the aerodynamic behavior predicted by the CFD simulations. The results shown correspond to a forward-flight case with a commanded pitch angle of $\alpha = 5°$ and a forward velocity of $V = 1.52\,\mathrm{m/s}$. These fields are used to support interpretation of pressure loading and momentum addition rather than as primary validation metrics.

Surface pressure coefficient. Elevated pressure levels are primarily concentrated near the central regions of the four arms of the drone, indicating localized stagnation and pressure loading. Away from these regions, the pressure distribution remains comparatively smooth over the simplified airframe surfaces, suggesting that the motor support structures are a dominant contributor to pressure drag in forward flight.

Velocity field. The velocity field shows elevated flow speeds in the regions of the BET disks, consistent with momentum addition from the rotors. In addition to the accelerated slipstream, the velocity vectors reveal the formation of two vortical structures upstream of the vehicle, located between the front motor pairs. These features indicate localized flow interaction induced by the forward-facing rotor arrangement and airframe geometry.

Mach number field. The Mach number distribution confirms that the flow remains in a low-Mach regime for the operating conditions considered. Localized increases in Mach number occur in regions of accelerated flow near the rotor slipstream, while the far field remains near the imposed freestream condition.

IV. Conclusions

This study validated a CFD-based blade element theory disk modeling approach against experimental flight data from a small quadrotor UAV. The results demonstrate that BET disk simulations accurately capture acceleration–velocity trends across multiple flight conditions while underpredicting absolute acceleration due to inherent modeling simplifications.

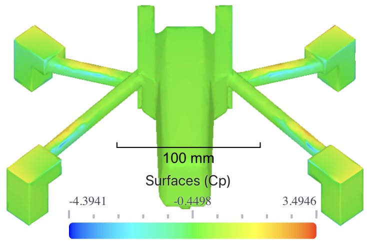

(a) Surface pressure coefficient

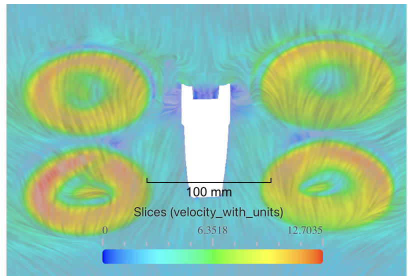

(b) Velocity slice

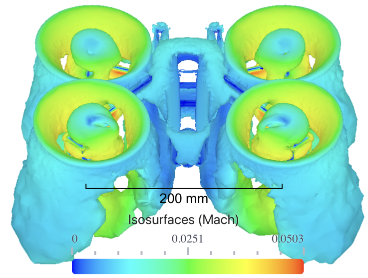

(c) Mach number field

Fig. 6 Representative flow-field visualizations for $\alpha = 5^\circ$ and $V = 1.52\,\mathrm{m/s}$, showing surface pressure coefficient, velocity magnitude slice, and Mach number distribution.

Comparison with a physics-based simulation environment further contextualized the results. These findings support the use of BET disk CFD methods as an efficient tool for early-stage UAV aerodynamic analysis and design validation.

Acknowledgment

The author would like to thank the team at Flexcompute—especially Runda, Jim, and Victor—for their continued guidance and support throughout this project, and Qiqi for providing the opportunity to pursue this work. AI was used to revise the writing of this paper.

References

[1] Glauert, H., *Airplane Propellers*, 2nd ed., Springer Berlin Heidelberg, Berlin, Heidelberg, 1935, pp. 169–360. https://doi.org/10.1007/978-3-642-91487-4_3, URL https://doi.org/10.1007/978-3-642-91487-4_3.

[2] Spalart, P. R., and Allmaras, S. R., "A One-Equation Turbulence Model for Aerodynamic Flows," *AIAA Paper 1992-0439*, 1992, p. 1.

[3] Jia, F., Spalart, P., Groom, M. J., and Wang, Q., "Fundamental studies towards rotor simulations and Design," *AIAA SCITECH 2023 Forum*, 2023. https://doi.org/10.2514/6.2023-2465.

[4] Moore, J., Wang, Q., and Jia, F., "XV-15 rotor simulation in Flow360 using the blade element theory," *Proceedings of the Vertical Flight Society 78th Annual Forum*, 2022, p. 1–9. https://doi.org/10.4050/f-0078-2022-17588.

[5] Jia, F., Moore, J., and Wang, Q., "Assessment of detached eddy simulation and sliding mesh interface in predicting tiltrotor performance in helicopter and airplane modes," *AIAA AVIATION 2021 FORUM*, 2021. https://doi.org/10.2514/6.2021-2601.